Supporting Information for: **"Interplay Between Microstructure, Defect States, and Mobile Charge Generation in Transition Metal Dichalcogenide Heterojunctions"**

Dana B. Sulas-Kern, Hanyu Zhang, Zhaodong Li, and Jeffrey L. Blackburn

National Renewable Energy Laboratory, Golden, CO 80401

Section S1. Experimental Methods

MoS_2 Chemical Vapor Deposition (CVD) Synthetic Methods.
   The MoS_2 growth procedures were adopted and modified from the previous methods developed by Yu and Liao et al.[1] The monolayer-only samples were prepared in the same batch as our previous report on MoS_2 kinetics in Reference 2. The multilayer-containing samples followed the same general procedure but were prepared in a different batch, which resulted in the growth of a small fraction of multilayer sections. The overall growth is a low-pressure growth with the assistant of O_2. Chemical vapor deposition (CVD) was performed in a three-temperature-zone furnace with a dedicated insert tube to supply 25 sccm Ar/O_2 (4 vol. % of O_2) premixing gas flow directly to Zone 2. Zone 1 contained 500 mg of sulfur (Sigma Aldrich), and the sapphire wafer (UniversityWafer) was located at Zone 3. 2 mg of MoO_3 (Sigma Aldrich) was loaded into the insert tube and placed into Zone 2 of the furnace. 125 sccm of Ar was supplied to the growth chamber to carry the sulfur and balance the growth pressure at 1 Torr. The precursor MoO_3 in the insert tube with O_2 flow can prevent the poison of the MoO_3 precursor. During the growth, Zone 1, 2, 3 had the temperature ramping-up speeds of 35, 35, and 70 °C/min, and maintained temperatures as 180, 530, and 930 °C, respectively, for 30 min. After monolayer MoS_2 growth, the samples were broken into smaller ~1 cm^2 pieces for further characterization and spectroscopic studies.

(6,5) Single-Walled Carbon Nanotube (SWCNT) Ink Preparation. Single-walled carbon nanotubes (SWCNTs, CoMoCAT SG65i, CHASM) were added in a concentration of 0.5 mg/mL to a solution of 2 mg/mL poly-[(9,9-dioctylfluorenyl-2,7-diyl)-*alt*-co(6,60-[2,20-bipyridine])] (PFO-BPy, American Dye Source) in toluene. The SWCNTs were dispersed using a Cole-Palmer CPX 750 tip sonicator with 0.5-inch diameter at 40% intensity for 15 minutes in a bath of flowing water. The dispersion was centrifuged for 5 minutes at 13,200 rpm and 20 °C in a Beckman Coulter L-100 XP ultracentrifuge with SW 32 Ti rotor to generate a compacted pellet and supernatant rich in (6,5) SWCNTs. The pellet was discarded, and the supernatant was centrifuged for an additional 16 hours at 24,100 rpm and 20 °C to generate a compacted pellet of (6,5) SWCNTs and supernatant containing excess PFO-BPy polymer. The supernatant was removed, and the (6,5) SWCNT pellet was gently rinsed with toluene before being redispersed in toluene using a heated ultrasonic bath sonicator. The polymer-removal centrifugation and subsequent redispersion were repeated twice.

SWCNT Spray Coating. MoS_2/SWCNT heterojunction films were prepared by spray coating the SWCNT ink onto MoS_2/sapphire substrates, and neat films were prepared by spray coating onto glass substrates that were cleaned by sequential sonication in acetone and isopropyl alcohol. The substrates were placed onto a motorized metal stage that was heated to 130 °C to evaporate solvent during the deposition. Prior to spray coating, the (6,5) SWCNT / PFO-BPy ink was diluted in toluene to reach an optical density of ~2.0 at the 1000 nm SWCNT S_{11} absorption peak. The ink was loaded into a syringe and injected at a rate of 0.3 mL/min through a SonoTek ultrasonic spray tip operated at 0.8 W. The

ink mist was directed toward the substrates by N_2 at a flow rate of 7.0 standard liters per minute, and the substrates were rastered beneath the mist to achieve 20-30 coats. The resulting films were soaked in toluene at 78 °C for 10 minutes to remove excess polymer.

Transient Absorption Spectroscopy. TA kinetics were characterized using pump-probe transient absorption spectroscopy. Pump pulses were generated with a tunable-wavelength Light Conversion Topas optical parametric amplifier using input from a Coherent Libra Ti:Sapphire laser (800 nm, 100 fs, 1 kHz). White-light supercontinuum probe pulses were generated by focusing a portion of the Ti:Sapphire output onto a sapphire plate. The pump-probe delay for the ultrafast time range (hundreds of femtosecond to 5.5 ns delay) was set using a mechanical translation stage prior to white light generation. Detection and data acquisition were carried out using the HELIOS system purchased from Ultrafast Systems Inc. For the nanosecond to microsecond time range, white-light probe pulses and electronic delays were generated using the EOS system purchased from Ultrafast Systems Inc. Samples for transient absorption measurements were isolated from atmosphere by mounting them inside a double-window chamber that was sealed inside a nitrogen glovebox.

Time-Resolved Microwave Photoconductivity. TRMC kinetics were characterized using pump-probe methods, where an optical pump and microwave probe were both incident on the sample located inside a custom-designed microwave cavity, where the cavity and set up are further described in great detail in Reference 3. To summarize: The 5 ns pump pulses were generated using a tunable-wavelength Continuum Panther optical parametric oscillator with input from the third harmonic of a Contiuum Powerlite Q-switched Nd:YAG laser at 355 nm. The probe was a microwave at around 9 GHz generated using a Silvers VO3262X/00 voltage-controlled oscillator. The microwave frequency was tuned by adjusting the voltage with a Keithley 230 source meter to minimize dark microwave reflection, and the change in microwave reflection caused by carrier photoexcitation by the pump pulse was detected using a 1N23C Schottkey barrier diode with the signal either amplified with a HAS-X-Z-40 (Femto GMBH) on the 500 ns timescale, or measured directly without amplification for the longer microwave timescale. The transients were recorded using an oscilloscope.

Steady-State Microwave photoconductivity. SSMC action spectra were recorded using lock-in detection by scanning through a range of wavelengths (chopped at 373 Hz) and measuring the change in reflected microwave power. The experimental setup is described in great detail in Reference 3. To summarize: The incident light was produced by a 150 W Xenon arc lamp with output passing through a OBB Tunable Power Arch monochromator with a 1200 l/mm grating. Order-sorting filters were used to eliminate artefacts from higher orders of incident light, and the power variations of the lamp/monochromator output were accounted for using a NIST-traceable calibrated Newport 818-UV silicon photodiode mounted at the sample position. Both the light and microwaves were incident on the sample within a custom-designed microwave cavity. The microwave probe was split to a create a sample probe and a reference, where each signal was detected by a matched 1N23C Schottky barrier diode. After using a Keithley sourcemeter to tune the microwave frequency to the resonance of the sample cavity in the dark (around 9.9 GHz), the sample and reference channels were tuned to have equal amplitude and 90º relative phase. The change in microwave power due to sample photoexcitation was recorded using a Teledyne LeCroy DA1855 differential voltage amplifier with inputs of the sample and reference signals, with the output recorded through a Stanford Research Systems SR830 lock-in amplifier referenced to the chopping frequency of the optical excitation. The action spectra in this study were processed assuming a bimolecular

recombination mechanism where $\dfrac{\varphi(\sum \mu)^2 F_A}{\gamma_r} = \dfrac{\Delta G^2 a^2}{I_0 q^2 b^2 d}$, as further described in Reference 3, where φ is the charge carrier yield per absorbed photon, μ is the carrier mobility, F_A is the fraction of absorbed light, γ_r is the bimolecular recombination rate constant, ΔG is the steady-state photoconductance measured in the SSMC experiment, a and b are the short and long dimensions of the waveguide cross section, I_0 is the incident photon flux, q is the elementary charge, and d is the sample thickness.

Steady-State Absorption Spectroscopy. Ground-state absorption spectra were recorded using a Varian Cary 5000 spectrophotometer in transmission mode with baseline correction.

Atomic Force Microscopy (AFM). MoS_2 height profiles and estimates of MoS_2 multilayer coverage were obtained using a Bruker Innova atomic force microscope in contact mode.

Raman and Photoluminescence Spectroscopy. Measurements were carried out using an inVia Renishaw confocal Raman microscope with a 532 nm laser and a 100x objective lens. Raman scattering was detected using a grating with 1800 lines/mm, and photoluminescence was recorded using a grating with 600 lines/mm.

Section S2. AFM Characterization of Multilayer-Containing Monolayer MoS_2

Figures S1-S3 show AFM images from three different areas of the multilayer-containing MoS_2 material, which we use to estimate the average size of multilayer islands and their coverage of the predominately-monolayer material. Tables S1-S3 show the particle analysis parameters. We estimate an average coverage of 0.8% by area, where the multilayer islands are on average 91.0 +/- 38.7 nm high and 358.5 +/- 97.9 nm in diameter.
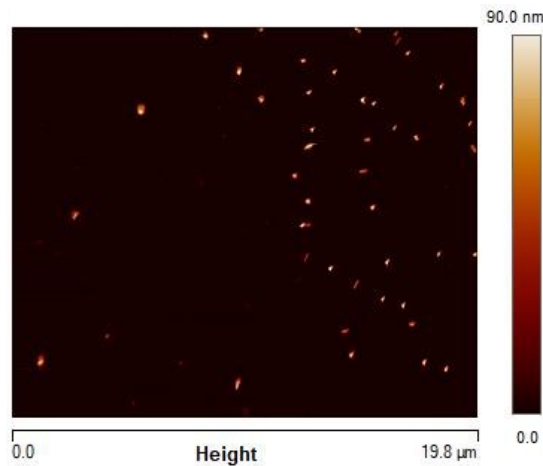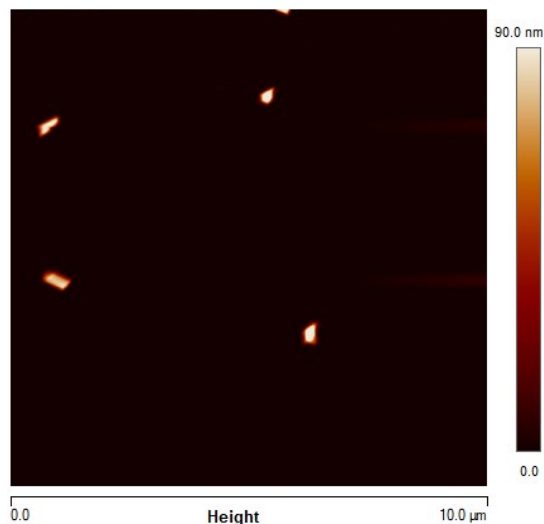

Figure S1. *AFM image showing distribution of multilayer islands, where the area coverage is ~0.85%.*

Table S1. *Particle Analysis Parameters from the AFM image in Figure S1*

	Mean	Minimum	Maximum	Sigma
Total Count	48.000	48.000	48.000	0.000
Number Density	0.145 (/μm²)	0.145 (/μm²)	0.145 (/μm²)	0.000 (/μm²)
Height	76.665 (nm)	14.453 (nm)	117.658 (nm)	22.633 (nm)

|				
Area of Particle	57768.871 (nm²)	10681.165 (nm²)	154495.422 (nm²)	28771.746 (nm²)
Diameter	263.603 (nm)	116.618 (nm)	443.520 (nm)	63.773 (nm)

Figure S2. *AFM image showing distribution of multilayer islands, where the area coverage is ~0.59%.*

Table S2. *Particle Analysis Parameters from the AFM image in Figure S2*

	Mean	Minimum	Maximum	Sigma
Total Count	4.000	4.000	4.000	0.000
Number Density	0.040 (/µm²)	0.040 (/µm²)	0.040 (/µm²)	0.000 (/µm²)
Height	108.327 (nm)	87.512 (nm)	125.539 (nm)	17.128 (nm)
Area of Particle	147724.156 (nm²)	108337.406 (nm²)	187683.109 (nm²)	28822.266 (nm²)
Diameter	431.587 (nm)	371.402 (nm)	488.841 (nm)	42.668 (nm)
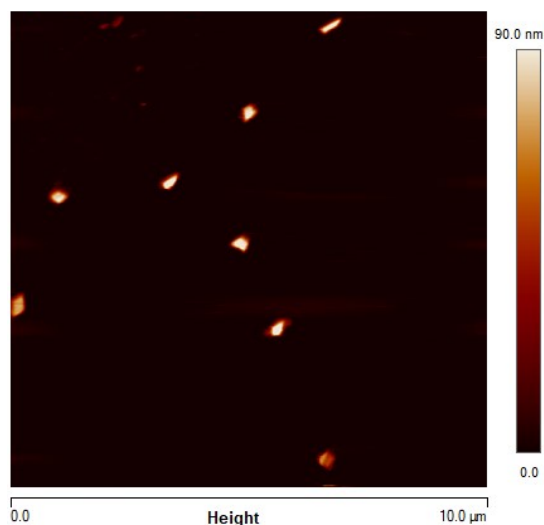
Figure S3. *AFM image showing distribution of multilayer islands, where the area coverage is ~1.0%.*

**Table S3.** *Particle Analysis Parameters from the AFM image in Figure S3*

	Mean	Minimum	Maximum	Sigma
Total Count	9.000	9.000	9.000	0.000

Number Density	0.090 (/μm²)	0.090 (/μm²)	0.090 (/μm²)	0.000 (/μm²)
Height	88.030 (nm)	28.601 (nm)	126.712 (nm)	26.373 (nm)
Area of Particle	116433.039 (nm²)	37384.031 (nm²)	152969.359 (nm²)	30886.623 (nm²)
Diameter	380.187 (nm)	218.172 (nm)	441.324 (nm)	60.869 (nm)

Figures S4-S6 show the AFM height profiles across scratches made with a razor blade in monolayer areas of the 0.8%-Multilayer MoS$_2$ material. The monolayer heights are indicated by gray dotted lines that give height values of 0.67 nm (Figure S4), 0.62 nm (figure S5), 0.74 nm (Figure S6). This is consistent with the ~0.7 nm height measured in the monolayer-only CVD-grown material.[2]
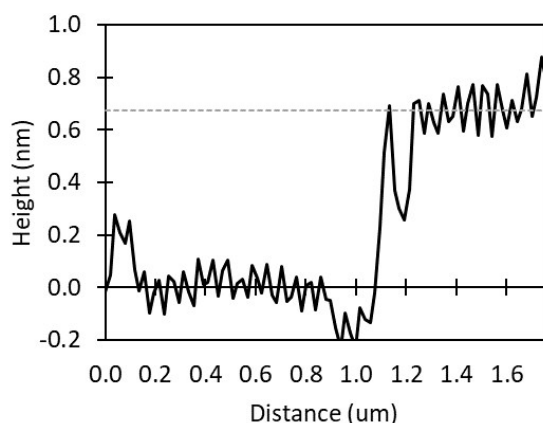
Figure S4. *AFM height profile for the 0.8%-multi MoS$_2$ sample in a monolayer area, showing monolayer height of ~0.67 nm.*
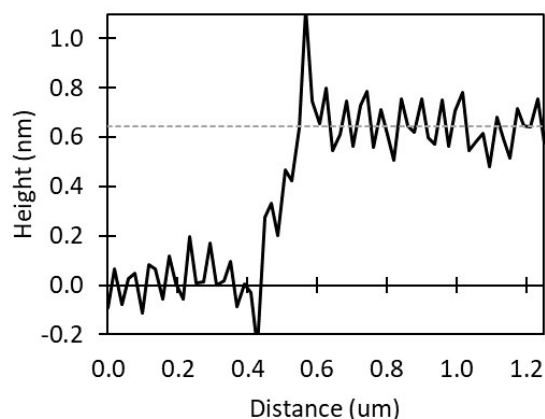
Figure S5. *AFM height profile for the 0.8%-multi MoS$_2$ sample in a monolayer area, showing monolayer height of ~0.62 nm*
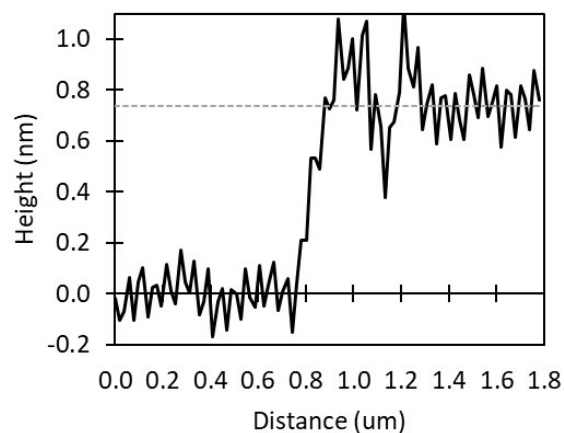
Figure S6. *AFM height profile for the 0.8%-multi MoS$_2$ sample in a monolayer area, showing monolayer height of ~0.74 nm.*

Section S3: Transient Absorption Fitting

Microsecond Timescale Charge Recombination

We fit the charge carrier recombination (Figure 2 of the main text) using a triple exponential decay for the TA data at 1175 nm, which corresponds to the SWCNT trion induced absorption. We report the amplitude-weighted average lifetime as $\tau_{CR} = (A_1\tau_1 + A_2\tau_2 + A_3\tau_3) / (A_1 + A_2 + A_3)$. Our results give average lifetimes of 4.71 μs for 0.8%-multi MoS_2/SWCNT and 0.73 μs for monolayer-only MoS_2/SWCNT. The fitting parameters for the 0.8%-multilayer MoS_2/SWCNT heterojunction are given in Table S4. The corresponding fit for the monolayer-only MoS_2/SWCNT heterojunction is given in Ref. 2.

Table S4. *Multi-Exponential fitting parameters*

A	τ (μs)	Amplitude Percent
0.27303	0.043224	30.2473
0.34611	0.93034	38.3433
0.28352	13.831	31.4094

Picosecond Timescale Charge Generation

We estimate the charge-transfer yield for the 0.8%-multilayer MoS_2/SWCNT heterojunctions using the same method described in Reference 2. The corresponding values for the monolayer-only MoS_2/SWCNT heterojunction are given in Reference 2. Using global target analysis, we separate the charge-associated TA component from the exciton-associated TA component as shown in Figure S7.[4] We find that the TA data in the NIR region can be fit using two spectra shapes: We assign the component with fast sub-picosecond decay to initially photoexcited excitons, and we assign the longer-lived spectrum that rises with ~0.5 ps time constant as the SWCNT charge signature. The charge-associated signature has an induced absorption at 1175 nm, which is characteristic of SWCNT trion induced absorption. As shown in the kinetic traces of Figure S7, three charge-associated components are needed to fit the data, but the spectral shape is the same for all three charge-associated components.
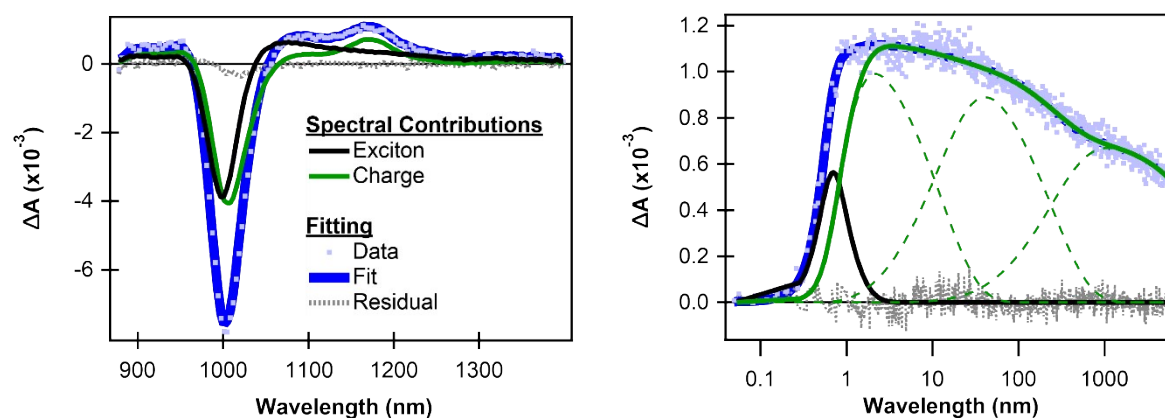
Figure S7. *Results of global target analysis[4] for the 0.8%-multilayer MoS_2/SWCNT heterojunction, showing fitting of the ΔA spectrum at 1ps (left), and fitting of the kinetic trace at 1175 nm (right).*

We estimate the charge-transfer yield using the charge-associated component when its intensity is maximized, which is at about 3 ps in Figure S7. We fit a gaussian curve to the trion induced absorption around 1175 nm, and we use the area under the curve to obtain the relative trion optical density of $OD(X^+)/OD(S_{11})$. We obtain the optical density of the S_{11} ground state absorption by fitting a gaussian curve

to the peak at 1000 nm in the steady-state absorption spectrum. We then use the relative trion optical density to find the photogenerated hole concentration using an empirically-determined relationship for the trion absorption cross section[5]

$$\frac{OD(X^+)}{OD(S_{11})} = 0.0674 - 0.0676 * Exp(-21.5\, N_h)$$
, (S1)

where N_h is the hole density nm^{-1} of tube length. We convert the units to cm^{-2} of pump area as

$$N_h[cm^{-2}] = N_h[cm^{-1}]\frac{OD_{S11}}{\sigma N_c}$$
(S2)

where the absorption cross section σ is 1.5 x 10^{-17} cm^2 atom^{-1} and the atomic density per nanometer of tube length N_C is 90.613 atoms nm^{-1}.[6] We then determine the charge-transfer yield as N_h/N_X, where N_X is the initial exciton concentration from the number of absorbed photons in the pump area (e.g. incident photons cm^{-2} * (1-10$^{-OD(S11)}$).

The gaussian fitting parameters used to determine OD(X^+)/OD(S_{11}) are given in Table S5. Two charge-associated components are included and scaled to represent their contribution to the total signal at the time when the charge-associated signal is maximized (~3ps).

Table S5. Fitting parameters used to calculate the relative optical density of the trion induced absorption

Electron Transfer Yield (1000 nm excitation) 0.8%-multi MoS₂/SWCNT		Hole Transfer Yield (440 nm excitation) 0.8%-multi MoS₂/SWCNT	
Charge Comp 1		**Charge Comp 1**	
y0	0	y0	0
A	1.73E-04	A	1.08E-03
xo	1174	xo	1170.6
width	31.604	width	47.088
area	1.37E-02	area	1.28E-01
adjusted for time trace	1.22E-02	adjusted for time trace	1.12E-01
Charge Comp 2		**Charge Comp 2**	
y0	0	y0	0
A	2.96E-04	A	1.04E-03
xo	1163.9	xo	1171.4
width	52.535	width	35.638
area	3.90E-02	area	9.27E-02
adjusted for time trace	3.28E-03	adjusted for time trace	8.34E-03
S11		**S11**	
y0	0	y0	0
A	1.61E-01	A	1.61E-01
x0	999.49	x0	999.49
width	33.4	width	33.4

area	1.35E+01
OD(X+)/OD(S11)	**1.15E-03**

area	1.35E+01
OD(X+)/OD(S11)	**8.95E-03**

Section S4: Long-lived MoS$_2$ Signal

Figure S8 shows an interesting observation where the red-shifted MoS$_2$ spectral signature discussed in the main text for 0.8%-multilayer MoS$_2$ samples persists past 100 µs, which is well past the decay of the SWCNT-related charge signature. In Figure S8, we show a comparison of the long-lived MoS$_2$ signature with the SWCNT S$_{22}$ bleach, but we note that this SWCNT S$_{22}$ decay time is similar to the SWCNT trion induced absorption that we show in the main text. This observation of a long-lived MoS$_2$ signature further supports our hypothesis that the MoS$_2$ material with 0.8% multilayer islands plays a key role in sustaining long-lived charge carriers, potentially where carriers on MoS$_2$ continue to persist even after SWCNT-located carriers have decayed.

We further note the interesting observation that the MoS$_2$ TA signal in Figure S8 shows similar kinetics between the heterojunction and neat material, while the microwave photoconductivity signal is clearly much longer-lived in the heterojunction. This observation might suggest that the TA signature represents a long-lived defect state that is similar between both the neat material and heterojunction, which is independent of exciton dissociation at the MoS$_2$/SWCNT heterojunction interface. The longer-lived microwave photoconductivity signal in the heterojunction likely indicates greater mobile carrier generation in the heterojunction when the defect states are occupied.
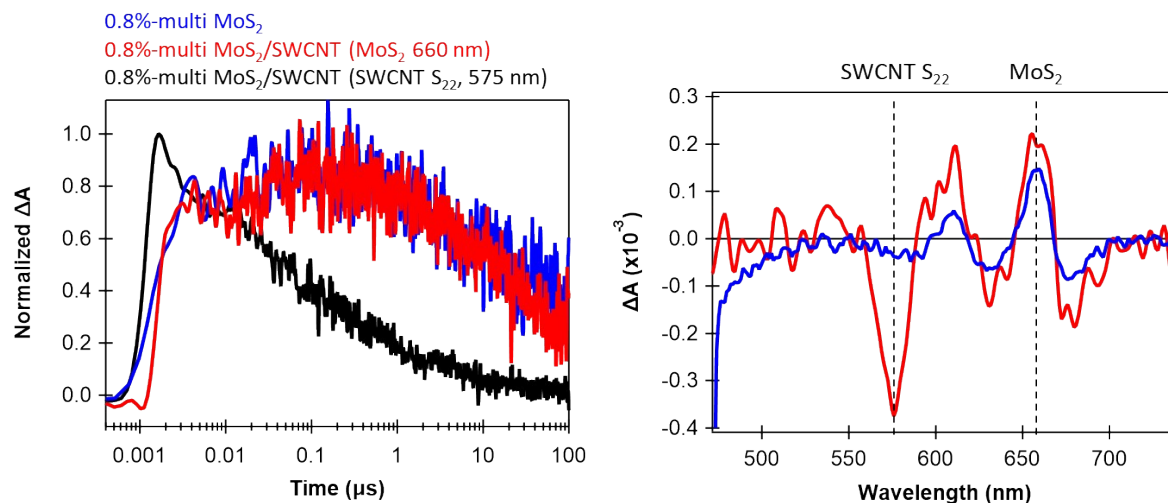
Figure S8. *Normalized transient absorption signals for MoS$_2$ at the 660 nm induced absorption and the SWCNTs at the 575 nm bleach (left), along with transient absorption spectral shapes averaged up to 0.3 µs (right).*

Figure S9 shows a comparison of the transient absorption spectral evolution between the neat 0.8%-multilayer MoS$_2$ and the neat monolayer-only MoS$_2$. Similar to the heterojunction samples shown in the main text (Figure 5), we observe the abrupt spectral shift for the 0.8%-multilayer MoS$_2$ around 10-100 ps, while the MoS$_2$ bleach positions in the neat monolayer-only MoS$_2$ remain near the same wavelength for this entire time window.
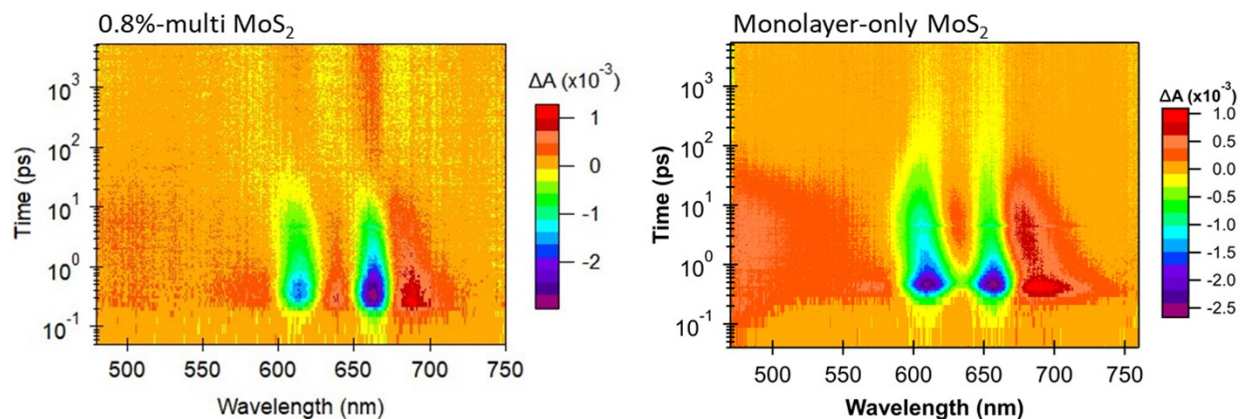
Figure S9. *Transient absorption comparing neat 0.8%-multilayer MoS$_2$ and neat monolayer-only MoS$_2$.*

Section S5: MoS$_2$ CVD-Grown Flakes

In the main text we discuss the effect of multilayer islands on large-area CVD-grown monolayer MoS$_2$. Importantly, we note that our observation of longer carrier lifetimes and red-shifted TA spectral signatures are **not** unique only to the samples discussed in the main text. In this section, we demonstrate the generality of this effect in a different set of predominately monolayer MoS$_2$/SWCNT samples.

The optical images in Figure S10 highlight the microstructure of the CVD-grown MoS$_2$ flakes, where these images represent different areas of the same substrate that had a gradient of varying MoS$_2$ flake sizes. Figure S11 shows the corresponding photoluminescence maps of areas with small MoS$_2$ flakes and large MoS$_2$ flakes. The Raman scattering in both cases (Figure S11c) shows that the samples are predominately monolayer MoS$_2$ with ~18.8 cm^{-1} energy difference between the E$^1_{2g}$ and A$_{1g}$ peaks.
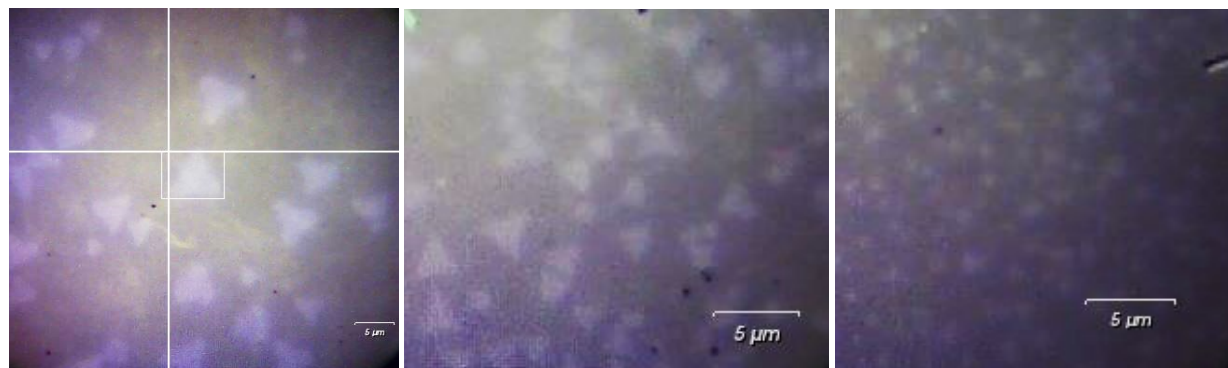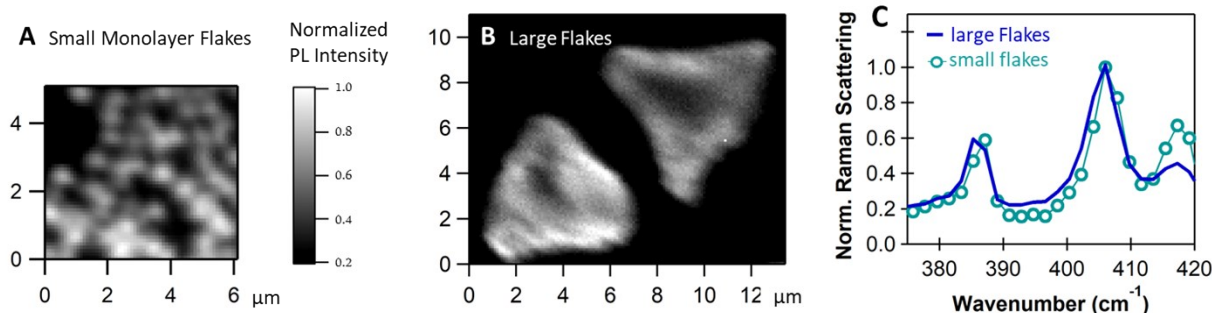

Large Flakes   Medium Flakes   Small flakes

***Figure S10.*** *Optical images of MoS$_2$ triangular flakes grown by CVD, where the scale bar is 5 µm in all images.*

Figure S11. *Photoluminescence (PL) maps at 660 nm corresponding to the monolayer MoS_2 A-exciton PL peak measured using 532 nm excitation for (a) small MoS_2 flakes and (b) large MoS_2 flakes; (c) Raman scattering at the MoS_2 E^1_{2g} and A_{1g} modes showing ~18.8 cm^{-1} peak difference which is typical for monolayer MoS_2.*

Interestingly, we find that the heterojunction containing large MoS_2 flakes exhibits the red-shifted MoS_2 bleach positions at 2-5 ns time delays (Figure S12a), similar to the 0.8%-multilayer sample in the main text (Figures 5a and 5c). We speculate that the abrupt TA shift may be due to higher defect density and/or a multilayer section within the large flakes, possibly making them a pyramid microstructure. In contrast, Figure S12b shows TA spectra for the MoS_2/SWCNT heterojunctions that contain the small monolayer-only MoS_2 flakes, where the MoS_2 bleach positions do not shift by a significant amount. We speculate that this is because the smaller flakes did not grow to a large enough size to support the growth of additional multilayer sections within the monolayer flakes. We note that, similar to 1L-only versus 0.8%-multilayer heterojunctions, the small flake versus larger flake MoS_2/SWCNT heterojunctions also show longer-lived charge carriers in the large-flake scenario where the abrupt MoS_2 spectral shift occurs (Figure S13). Taken together, these results demonstrate an abrupt MoS_2 spectral shift that appears related to microstructure and correlated with longer-lived charge generation.
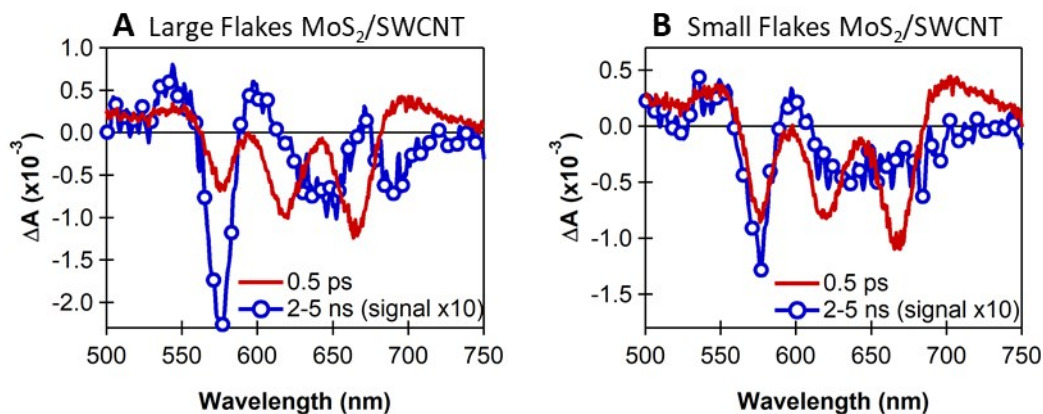

Figure S12. *Transient absorption spectra with 440 nm excitation at 1.2 x 10^{12} absorbed photons cm^{-2} at 0.5ps (red traces) and averaged over 2-5 ns (blue circles) for MoS_2/SWCNT heterojunctions containing either (a) large MoS_2 flakes or (b) small MoS_2 flakes.*
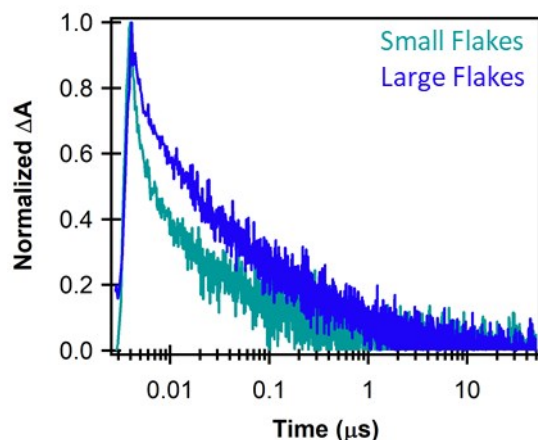
Figure S13. *Transient absorption kinetics at the SWCNT trion induced absorption (1175 nm) for MoS$_2$/SWCNT heterojunctions containing either small MoS$_2$ flakes (light blue) or large MoS$_2$ flakes (dark blue), demonstrating longer carrier lifetimes in heterojunctions with large flakes.*

Section S6: Comparison of TA line-shape with Absorption Derivatives

Figure S14 shows that the long-lived TA line-shape in the samples containing 0.8%-multilayer MoS$_2$ cannot be reconstructed from the first or second derivatives of the ground-state absorption.
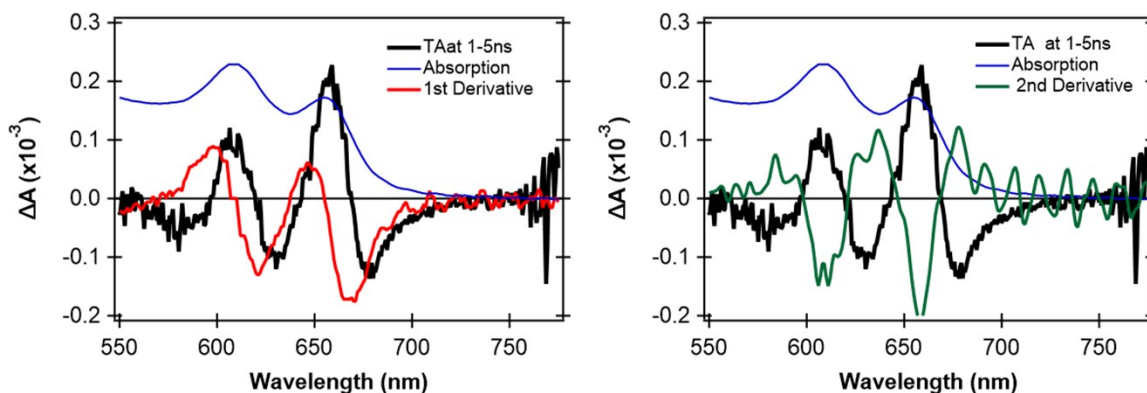
Figure S14. *Comparison of the long-lived TA spectral signature in 0.8%-multilayer MoS$_2$ with the first and second derivative of the MoS$_2$ steady-state absorption spectrum.*

References

1. Yu, H.; Liao, M.; Zhao, W.; Liu, G.; Zhou, X. J.; Wei, Z.; Xu, X.; Liu, K.; Hu, Z.; Deng, K.; Zhou, S.; Shi, J.-A.; Gu, L.; Shen, C.; Zhang, T.; Du, L.; Xie, L.; Zhu, J.; Chen, W.; Yang, R.; Shi, D.; Zhang, G., Wafer-Scale Growth and Transfer of Highly-Oriented Monolayer MoS2 Continuous Films. *ACS Nano* **2017,** *11* (12), 12001-12007.
2. Sulas-Kern, D. B.; Zhang, H.; Li, Z.; Blackburn, J. L., Microsecond Charge Separation at Heterojunctions Between Transition Metal Dichalcogenide Monolayers and Single-Walled Carbon Nanotubes. *Materials Horizons* **2019**.
3. Reid, O. G.; Moore, D. T.; Li, Z.; Zhao, D.; Yan, Y.; Zhu, K.; Rumbles, G., Quantitative analysis of time-resolved microwave conductivity data. *J. Phys. D: Appl. Phys.* **2017,** *50* (49), 493002.

4.   Snellenburg, J. J.; Laptenok, S.; Seger, R.; Mullen, K. M.; van Stokkum, I. H. M., Glotaran: A Java-Based Graphical User Interface for the R Package TIMP. *J. Stat. Softw.* **2012,** *49* (3), 1-22.

5.   Dowgiallo, A.-M.; Mistry, K. S.; Johnson, J. C.; Blackburn, J. L., Ultrafast Spectroscopic Signature of Charge Transfer between Single-Walled Carbon Nanotubes and C60. *ACS Nano* **2014,** *8* (8), 8573-8581.

6.   Blackburn, J. L.; Ferguson, A. J.; Reid, O. G., Spectroscopy of Ground- and Excited-State Charge Carriers in Single-Wall Carbon Nanotubes. In *Handbook of Carbon Nanomaterials*, World Scientific: 2017; Vol. Volume 9 & 10, pp 237-296.